Journal of Environmental Chemical Engineering 12 (2024) 113822

Contents lists available at ScienceDirect

Journal of Environmental Chemical Engineering

journal homepage: www.elsevier.com/locate/jece

Experimental and theoretical investigation of the treatment of Cu-rich Acid Mine Drainage using iron oxide magnetic nanoparticles

Nelson Naveas [a,b,c,*,1], Ruth Pulido [c,d], Teófilo Graber [b], Raúl Martin-Palma [a,c], Fernando Agulló-Rueda [e], Iván Brito [d], Miguel Ángel García [f], María Teresa Sevilla [g], Jacobo Hernández-Montelongo [h], Álvaro Muñoz-Noval [i,j], Carlo Marini [k], Leonardo Soriano [a,c], Jorge Sánchez-Marcos [l], Miguel Manso-Silván [a,c,m]

[a] Departamento de Física Aplicada, Universidad Autónoma de Madrid, Madrid 28049, Spain
[b] Departamento de Ingeniería Química y Procesos de Minerales, Universidad de Antofagasta, Avenida Angamos 601, Antofagasta, Chile
[c] Instituto Universitario de Ciencia de Materiales "Nicolás Cabrera" (INC), Universidad Autónoma de Madrid, Campus de Cantoblanco, Madrid 28049, Spain
[d] Departamento de Química, Universidad de Antofagasta, Avenida Angamos 601, Antofagasta, Chile
[e] Instituto de Ciencia de Materiales de Madrid (ICMM), Campus de Cantoblanco, Madrid 28049, Spain
[f] Instituto de Cerámica y Vidrio, CSIC, C/ Kelsen n 5, Campus de Cantoblanco, Madrid 28049, Spain
[g] Departamento de Química Analítica y Análisis Instrumental, Universidad Autónoma de Madrid, Madrid 28049, Spain
[h] Departamento de Ciencias Matemáticas y Físicas, UC Temuco, Temuco 4813302, Chile
[i] Departamento Física de Materiales, Universidad Complutense, Avenida Complutense, s/n, Madrid E-28040, Spain
[j] IMDEA Nanociencia, C/Faraday 9, Madrid E-28049, Spain
[k] ALBA Synchrotron Light Source, Carretera BP 1413, Km. 3.3, Cerdanyola del Vallés, Barcelona 08290, Spain
[l] Departamento de Química Física Aplicada, Universidad Autónoma de Madrid, Madrid 28049, Spain
[m] Centro de Microanálisis de Materiales, Universidad Autónoma de Madrid, Campus de Cantoblanco, Madrid 28049, Spain

ARTICLE INFO

Keywords:
Acid Mine Drainage (AMD)
Magnetic nanoparticles (MNP)
Magnetite (Fe_3O_4)
Maghemite (γ–Fe_2O_3)
Density Functional Theory
DFT + U

ABSTRACT

Acid Mine Drainage (AMD) is a significant environmental problem in the mining industry due to its high concentration of hazardous metals and metalloids, sulfate compounds, and low pH levels. Despite the attention that iron oxide magnetic nanoparticles (MNP) have received for AMD remediation, there is still a lack of understanding of the physicochemical mechanisms behind their non-specific adsorption, particularly in distinct variations of AMD, such as Cu-rich AMD. In this study, we synthesized, characterized, and applied MNP to the two-step treatment of Cu-rich AMD. The chemical and physical properties of the MNP and magnetically separated sludges after AMD treatment are characterized. Additionally, the chemical species adsorbed onto the MNP, the oxidation state of the resultant sludge after Cu-rich AMD treatment, and the short-range ordering of metal contaminant species on the surface of the MNP are identified. Finally, first-principles calculations using Density Functional Theory were conducted to understand how different Cu ion species adsorb to the MNP surface depending on the pH of the Cu-rich AMD. The bonding between MNP and Cu species occurs primarily through metal cation-oxygen bonds on the surface of MNP, and this bonding is influenced by the pH of the solution. A combination of experimental and theoretical approaches was the key to arrive at this conclusion. This information can aid in the comprehension of how metal contaminants adhere to the surfaces of MNP and in the precise engineering of these nanoparticles.

1. Introduction

It is known that the mining industry has been a fundamental pillar in the development of our global economy. However, despite its great economic benefits, mining activities have produced considerable solid and liquid hazardous waste. In particular, acid mine drainage (AMD), also known as acid rock drainage (ARD), is a highly significant environmental problem in this industry [1]. It is typically characterized by

* Corresponding author at: Departamento de Física Aplicada, Universidad Autónoma de Madrid, Madrid 28049, Spain.
E-mail address: nelson.naveas@estudiante.uam.es (N. Naveas).
[1] ORCID(s): 0000-0001-7511-2910.

https://doi.org/10.1016/j.jece.2024.113822
Received 1 April 2024; Received in revised form 4 August 2024; Accepted 12 August 2024
Available online 14 August 2024

Table 1
Application of MNP for the treatment of the simulated Cu-rich AMD.

		Metal concentration (mg/l)								
Sample	pH	Ca	Cu	Mg	Na	Co	Zn	Fe	Al	K
AMD	2.9	156 ± 5	691 ± 25	223 ± 5	32 ± 2	0.54 ± 0.03	7.2 ± 0.1	46 ± 0.1	137 ± 5	92 ± 1.1
MNP	2.9	148 ± 3	558 ± 12	215 ± 6	34 ± 1	0.52 ± 0.02	6.2 ± 0.5	45 ± 0.9	136 ± 3	90 ± 0.6
NH_4OH*	6.0	158 ± 6	289 ± 11	210 ± 7	34 ± 2	0.54 ± 0.01	4.8 ± 0.3	< LoD	< LoD	88 ± 0.5
MNP + NH_4OH	6.0	153 ± 7	205 ± 8	199 ± 5	36 ± 2	0.47 ± 0.02	5.2 ± 0.3	< LoD	< LoD	91 ± 0.2

< LoD: Below the detection limits.
* Basification control. To evaluate the effect of basification alone, without the presence of MNP.

the high concentration of heavy metals and metalloids (such as As, Sb, Cu, Pb, Cd, Zn, Hg, Ag, Sn, Fe, Al, Mn, Tl, U, Th, and W), sulfate compounds, and low pH levels [2].

AMD is produced through the oxidation of sulfide minerals by air and water and is accelerated by bacterial activity. Thus, solid mining waste, such as tailings containing sulfide minerals, pyrite (FeS_2) for instance, is prone to AMD formation through a complex process involving chemical, biological, and electrochemical reactions [3]. The resultant acid from these chemical reactions leaches heavy and toxic metals from the solid medium to the AMD, causing negative effects on different systems.

In particular, AMD originating from copper mines contains high concentrations of Cu ions, often accompanied by elevated levels of Fe^{2+}/Fe^{3+} ions as a result of bacterial leaching of copper sulfide and iron minerals. For instance, the mineral chalcopyrite ($CuFeS_2$) can undergo oxidation in acidic conditions as shown in the following overall reaction [4], producing Cu-rich AMD:

$$CuFeS_2 + 4H^+ + O_2 \Rightarrow Cu^{2+} + Fe^{2+} + 2S^0 + H_2O \quad (1)$$

Although various methods for mitigating the negative consequences of AMD have been studied, including conventional methods utilizing neutralizing agents (e.g., limestone, lime, and other reagents) as well as passive methods (e.g., geochemical and biological treatment) [1,5–7], research on the treatment of Cu-rich AMD is less well studied. In this sense, a limited number of studies have concentrated on the treatment of Cu-rich AMD, investigating a range of methods, including chemical precipitation, ion exchange, membrane separation processes, and bioremediation [8–11]. Nevertheless, these treatment methods have been found to have certain limitations, including the use of high chemical agents and energy consumption, the generation of high levels of hazardous waste, and the necessity for AMD pre-treatments [3,12]. For this reason, the mining industry needs to find new environmentally friendly processes to recover and/or treat AMD. This process implies combining new strategies and concepts, such as industrial ecology, clean production, green chemistry, life cycle assessment, and sustainable engineering [13–15]. In this sense, nanotechnology can provide added value to the AMD issue in the mining industry. Nanotechnology strongly influences the development of advanced materials, which possess new properties and can be applied in different fields, including environmental engineering. In particular, the synthesis, characterization, and application of various iron oxide nanoparticles for treating industrial wastewater, including AMD, have received significant attention [16]. For example, iron oxide magnetic nanoparticles (MNP), such as Fe_3O_4 and $CoFe_2O_4$, have been used as seeds for AMD treatment [13]. Also, magnetic hydrogels with functionalized MNP have been used for removing metal contaminants from AMD-affected stream waters [14]. All of these systems share common features such as small particle sizes, high specific surface area, and ferromagnetic properties. Thus, they exhibit excellent capacities for contaminant removal, low environmental toxicity, and quick and easy separation from waste. However, despite the considerable attention MNP has received for environmental applications, the underlying physicochemical mechanism responsible for the exhibited non-specific adsorption has not yet been identified, especially for Cu-rich AMD. Several mechanisms have been proposed for the action of MNP, such as physical adsorption, surface complexation, ion exchange, and hard/soft acid-base interaction [15]. However, debate still needs to be addressed, such as which mechanisms control the process. Therefore, to understand the mechanisms of the adsorption of metallic species on the surface of MNP, it is necessary to determine the chemistry of the MNP surface by identifying the adsorbed species and any chemical reaction that may have taken place during the adsorption. In this sense, combining experimental and theoretical investigations, such as Density Functional Theory (DFT), can provide valuable insights into treating Cu-rich AMD using MNP.

In the present study, MNP was synthesized by the simple co-precipitation method and further applied in a two-step process to the Cu-rich AMD treatment. We exhaustively characterize the MNP and their magnetically separated sludges after the Cu-rich AMD treatment in terms of chemical and physical properties. Additionally, a first-principle calculation study via DFT was conducted to explain the underlying mechanism involved in the Cu-rich AMD treatment. With the recovered information, MNP can be engineered to design and optimize AMD treatment.

2. Materials and methods

2.1. Chemicals

The substances and standards utilized in this study are of analytical grade (purity ≥ 99 %). $FeSO_4 \cdot 7H_2O$, $FeCl_3 \cdot 6H_2O$, Na_2SO_4, $CuSO_4 \cdot 5H_2O$, $Al_2(SO_4)_3 \cdot 18H_2O$, $ZnSO_4 \cdot H_2O$, $MgSO_4 \cdot 7H_2O$, $CoSO_4 \cdot 7H_2O$, $CaCl_2 \cdot 2H_2O$, and KCl, were acquired from Merck Millipore®. NH_4OH (28–30 %) and HCl (37 %) were acquired from Sigma-Aldrich®. The solutions were made using ultrapure water obtained from the Milli-Q system ®, which has a resistivity of 18.2 $\mu\Omega \cdot$ cm. All the chemicals were used as received without further treatment.

2.2. Synthesis of iron oxide MNP

The MNP was synthesized utilizing an air-exposed co-precipitation method, as previously described by Kefeni [13], which differs slightly from traditional synthesis methods that use inert gas atmospheres. The Fe^{2+} and Fe^{3+} precursor solutions were prepared by dissolving 2.5 g of $FeSO_4 \cdot 7H_2O$ and 4.87 g of $FeCl_3 \cdot 6H_2O$ in 150 mL of ultrapure water. The two salts solutions were mixed in molar ratio R= $Fe^{3+}/Fe^{2+} = 2$ for 10 min. The solution was dropped with NH_4OH (28–30 %) to regulate pH to 9 and mechanically stirred at 60 °C. After two hours, the mixture was left to cool until it reached room temperature. The precipitate was washed multiple times with ultrapure water and magnetically separated. Ultimately, the resulting material was dried at 105 °C for six hours.

2.3. Cu-rich AMD treatment

The synthetic Cu-rich AMD solution is based on the chemical composition of a stream draining from a Chilean copper mine in the Atacama Desert (Table 1) [17]. Cu-rich AMD solution was prepared by dissolving appropriate amounts of Na_2SO_4, $CuSO_4 \cdot 5H_2O$, $Al_2(SO_4)_3 \cdot 18H_2O$, $FeSO_4 \cdot 7H_2O$, $ZnSO_4 \cdot H_2O$, $MgSO_4 \cdot 7H_2O$, $CoSO_4 \cdot 7H_2O$, $CaCl_2 \cdot 2H_2O$ and KCl in ultrapure water. To determine the metal

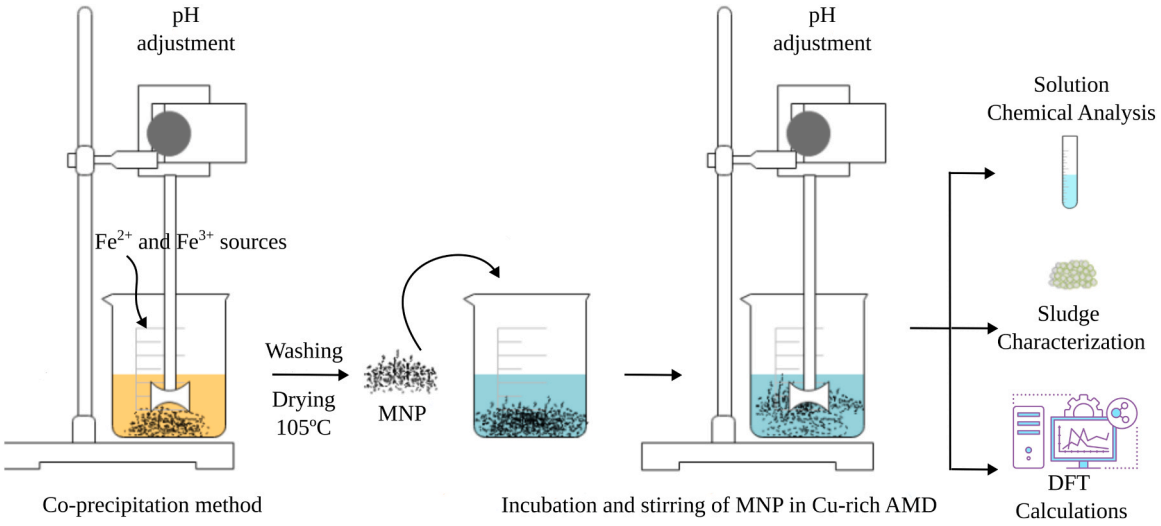

Fig. 1. Schematic representation of the MNP synthesis and its application to Cu-rich AMD treatment.

contaminant removal, 100 mL of synthetic Cu-rich AMD solution was treated by adding different masses of the MNP in a batch system under mechanical stirring for 24 h at 30 ˚C. To assess the potential for metal contaminant removal, we tested pH levels of 2.9 and 6.0. These pH levels were chosen to mimic the acidic conditions commonly found in Cu-rich AMD and to evaluate treatment under more neutral conditions. After the AMD treatment, the resulting material was magnetically separated, obtaining the solid part (here called sludge) and the supernatant, both available for physicochemical characterization. A schematic representation of the MNP synthesis, application, and characterization of the resultant materials is shown in Fig. 1. The experimental data for Cu adsorption on MNP were fitted using the non-linear form of the pseudo-second-order (PSO) kinetic model, as follows:

$$q_t = \frac{q_e^2 k_2 t}{1 + q_e k_2 t} \tag{2}$$

where q_t is the amount of adsorbate adsorbed at time t (mg/g), q_e is the amount of adsorbate adsorbed at equilibrium (mg/g) and k_2 is the rate constant of pseudo-second-order adsorption (g/mg · min).

2.4. Characterization techniques

The crystalline structure of the MNP and sludges samples was analyzed using powder X-ray diffraction (XRD). High-resolution transmission electron microscopy (HR-TEM) was used to study the morphology and microstructure of the MNP. Moreover, sludge samples were subjected to morphological and chemical analysis using a scanning electron microscope equipped with energy-dispersive X-ray analysis (SEM-EDX). The identification of functional groups in samples was accomplished using Fourier-transformed infrared (FT-IR) spectroscopy and Raman spectroscopy (RS) at ambient temperature. X-ray photoelectron spectroscopy (XPS) was utilized to determine the chemical composition of the surface of the MNP and its sludge after the two-step treatment. Mössbauer spectra (MS) were recorded at room temperature to provide information on the chemical and structural nature of the MNP. The specific surface area of MNP was determined by employing the multiple-point Brunauer - Emmett - Teller (BET) method. In order to determine the magnetic properties of the synthesized MNP, vibrating sample magnetometry (VSM) was used. X-ray absorption spectroscopy (XAS) studies were carried out at the CLÆSS beamline of the ALBA CELLS synchrotron facility in Spain. In this study, we examined both the X-ray absorption near-edge structure (XANES) and extended X-ray absorption fine structure (EXAFS) regions for Fe and Cu. The chemical composition of liquid samples was measured by using inductively coupled plasma optical emission spectroscopy (ICP-OES) and atomic absorption spectroscopy. For detailed information on characterization techniques, please refer to Section 1 of the supplementary material.

2.5. Calculations details

The DFT calculations were conducted utilizing the plane-wave (PW) pseudopotential methodology contained in the QUANTUM ESPRESSO computing software [18]. GGA-PBEsol PAW pseudopotentials were obtained from both the SSSP pseudopotential library [19] and the PSlibrary [20]. The Fe_3O_4 bulk crystal structure was optimized using the BFGS quasi-newton algorithm by the Hubbard-corrected method (DFT + U) using non-orthogonalized atomic orbitals [21,22]. The DFT + U approach was implemented using the simplified rotational-invariant formulation developed by Cococcioni and de Gironcoli [23] using a Hubbard U correction on Fe-3d states of 3.5 eV. Convergence thresholds of at least 1×10^{-4} Ry for total energy, 1×10^{-3} Ry/Bohr for forces, and 0.5 kbar for pressure were specified. For the bulk calculations, the conventional unit cell comprising 56 atoms was used, and the reciprocal space was sampled with a $4 \times 4 \times 4$ k point mesh. Kinetic-energy cutoff of 65 Ry for the wave function and 780 Ry for the charge density were used. During the computational analyses, we carefully considered the ferrimagnetic properties of Fe_3O_4 and the orientation of its spins. This focus was due to the strong antiferromagnetic interaction between the iron ions located in the tetrahedral (Fe_{tet}) and octahedral (Fe_{oct}) sites. As a result, the spins of the Fe_{oct} and Fe_{tet} ions are aligned in opposite directions [22].

The optimized bulk lattice parameter and atomic positions were used to build the $Fe_3O_4(001)$ surface model. For Fe_3O_4, the arrangement of atoms in the [001] direction is characterized by a stacking sequence composed of layers designated as A, which contain Fe_{tet}, and layers designated as B, which consist of oxygen and Fe_{oct} atoms. Here, we used termination B of the Fe_3O_4 surface for our analysis because previous observations have indicated that termination B is more stable than termination A [24–26]. The surfaces are represented as slabs, periodically repeated in the z-direction. To eliminate its periodic interactions in the z-direction, a vacuum layer of at least 12 Å was inserted along the c-axis. The slab model used eight atomic layers for the (001) termination in the structure optimization. The four topmost atomic layers and the adsorbed metal atom were fully relaxed, while the bottom four atomic layers were kept fixed. The adsorption strength is described by the adsorption energy (E_{ads}):

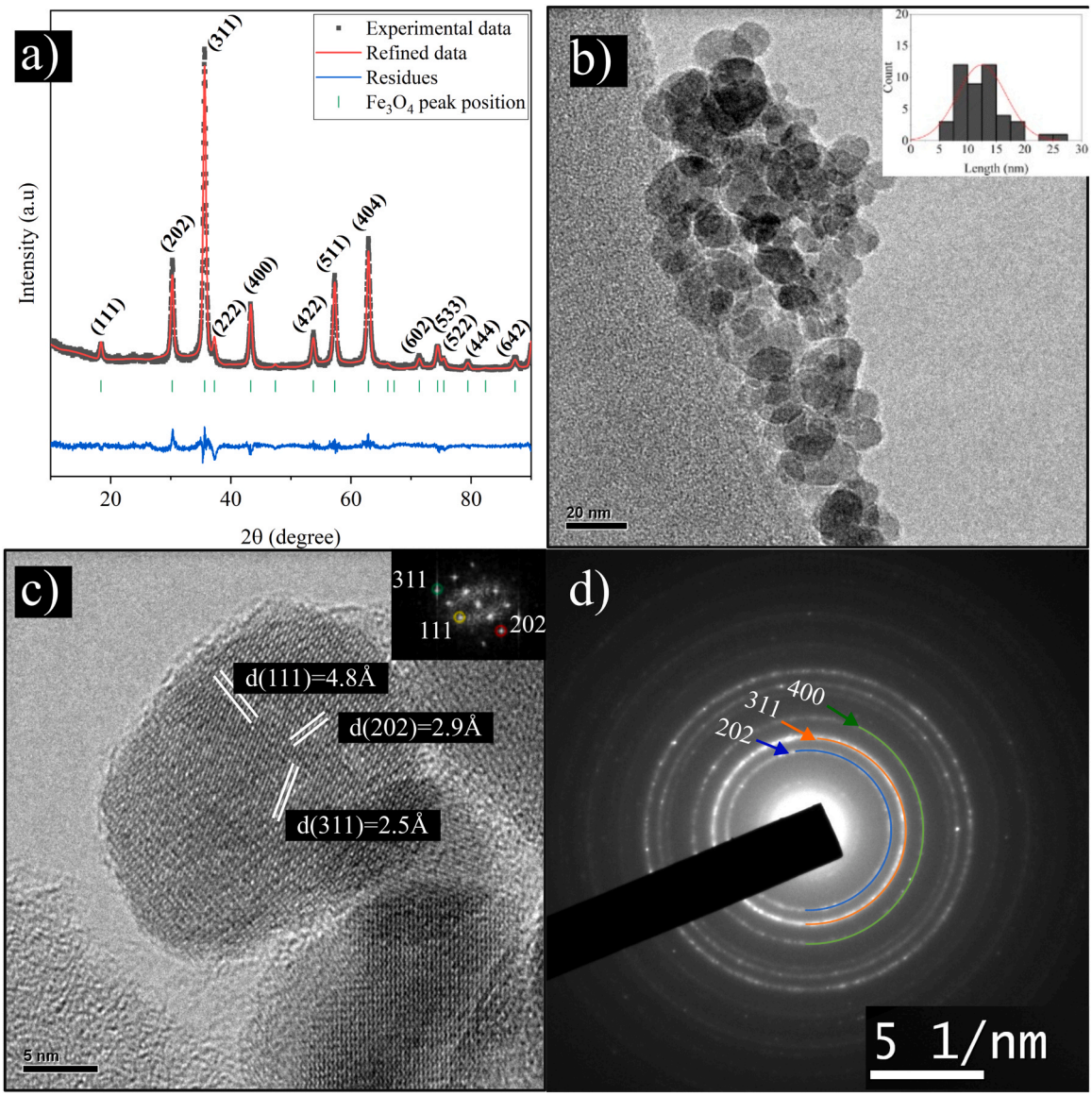

Fig. 2. (a) XRD patterns and Rietveld refinement of the MNP synthesized in this study. (b) TEM image and particle size distribution of the MNP (inset image), (c) HR-TEM image and FFT pattern (inset image) of Fe_3O_4 nanoparticle, and (d) SAED patterns of MNP.

$$E_{ads} = E_{adsorbate/slab} - [E_{adsorbate} + E_{slab}] \quad (3)$$

where $E_{adsorbate/slab}$, $E_{adsorbate}$ and E_{slab} are the energies of the adsorbed slab, a free adsorbate specie and the clean slab, respectively. Negative adsorption energy corresponds to a thermodynamically favorable interaction.

3. Results and discussion

3.1. MNP synthesis and characterization

To determine the crystal structure of the synthesized iron oxide MNP, the samples were analyzed by XRD. XRD and Rietveld refinement analysis showed that a single phase can be indexed from the diffraction patterns (Fig. 2a). As shown in Fig. 2a, peaks at 2θ angles of 18.34°, 30.24°, 35.63°, 37.30°, 47.41°, 53.72°, 57.27°, 62.90°, 71.37°, 74.43°, 75.44°, 79.44°, and 87.29° with their corresponding diffraction indices of (111), (202), (311), (222), (400), (422), (511), (404), (602), (533), (622), (444) and (642) confirmed the formation of the cubic spinel Fe_3O_4 (COD entry #9002319) [27]. Interestingly, weak peaks suggested the presence of the cubic maghemite (γ-Fe_2O_3) at 23.87° and 26.18°, with corresponding diffraction indices of (201) and (211) (COD entry #9006317) [28], as a residual phase. However, the content of this second phase was so small that it is impractical to perform a Rietveld refinement analysis with both phases. It is important to mention that it is difficult to distinguish Fe_3O_4 and γ-Fe_2O_3 by XRD because they possess the same spinel structure with almost identical lattice parameters. However, due to the order of cation vacancies, the diffraction patterns of γ-Fe_2O_3 present some weak additional peaks at low 2θ angles. In fact, the identification and quantification of Fe_3O_4-γ-Fe_2O_3 mixture has been previously reported [29]. Additionally, it is important to note that due to the conditions in our synthesis (air-exposed co-precipitation method), the formation of γ-Fe_2O_3 as a residual phase by oxidation of Fe_3O_4 to γ-Fe_2O_3 under atmospheric oxygen is plausible. Conversely, it is crucial to emphasize that no other peaks related to other iron oxide phases, like hematite (α-Fe_2O_3), were identified.

The cell parameters obtained from the Rietveld refinement of the Fe_3O_4 present in our MNP are presented in Table S1. Table S1 also shows the crystallite size analysis from XRD patterns using the Scherrer model, which resulted in an average crystallite size of 22 nm. Additionally, the

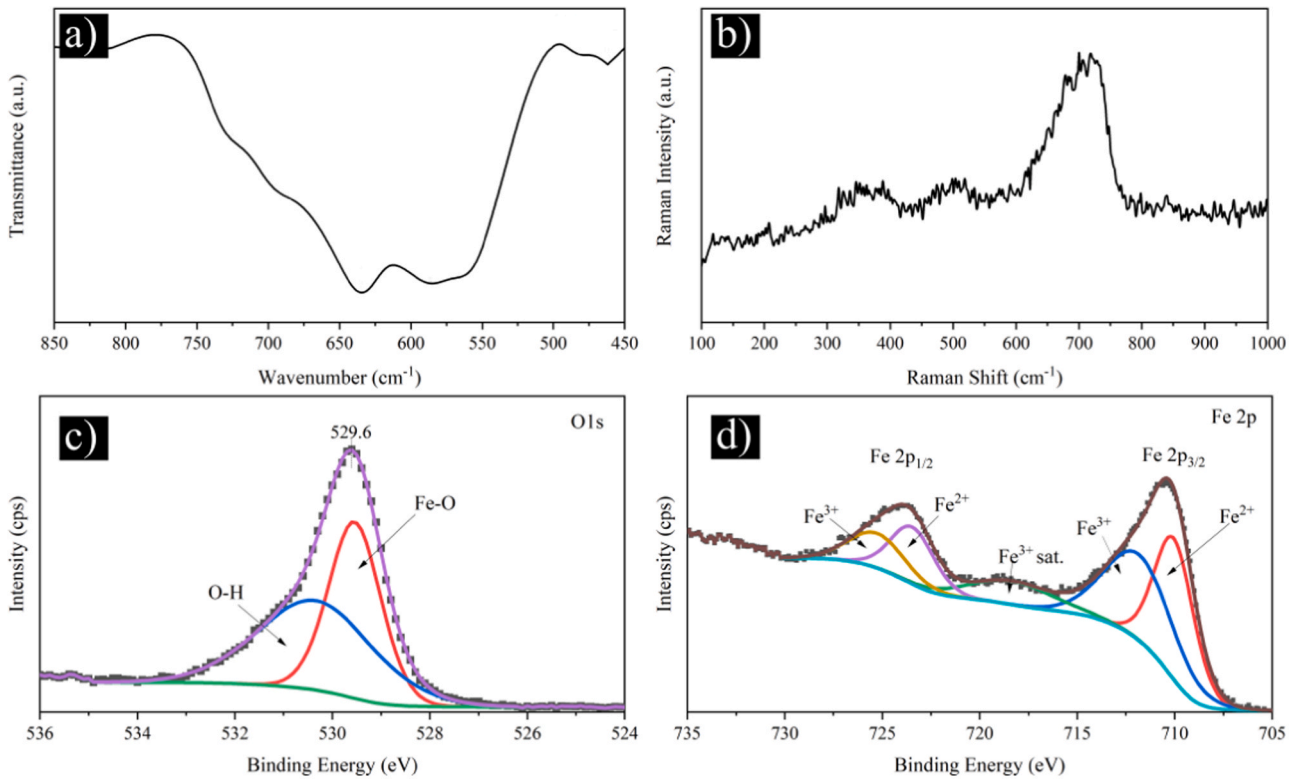

Fig. 3. (a) FTIR and (b) Raman spectra of the MNP used in this work. (c) O 1*s* and (d) Fe 2*p* high-resolution XPS spectra from MNP.

Table 2
Kinetic parameters for the Cu adsorption during the treatment of the Cu-rich AMD by MNP. Here, q_e represents the amount of Cu adsorbed at equilibrium and K_2 is the PSO rate constant.

	PSO kinetics		
pH	q_e	K_2	R^2
2.9	134.77 ± 1.42	0.009	0.99
6.0	487.64 ± 0.50	0.002	0.99

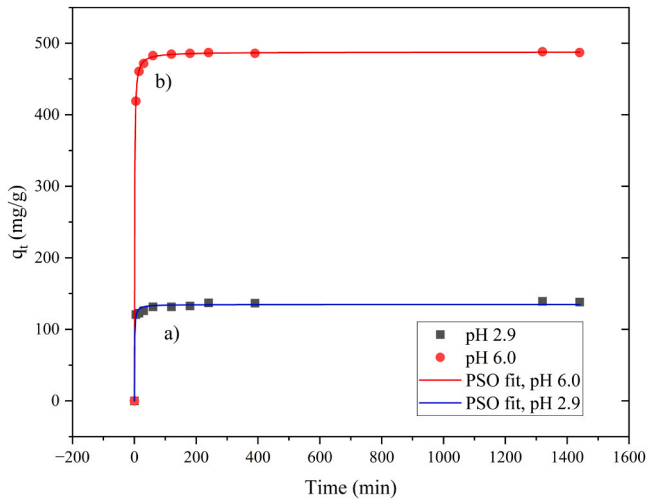

Fig. 4. Fitting of the PSO kinetics model to experimental data of Cu adsorption from Cu-rich AMD onto MNP at (a) pH 2.9 and b) pH 6.0. Here, the symbol q_t represents the amount of Cu that has been adsorbed at a given time t.

BET surface analysis showed a value of 82.55 m^2/g.

TEM and HR-TEM were subsequently used to identify the nanoscale morphology and local microstructure of the MNP (Fig. 2b–d). Fig. 2b shows the TEM image and the particle size distribution of the MNP. The MNP exhibited agglomerates of granular morphologies and crystallite sizes of about 12 ± 4 nm. Figs. 2c and d show HR-TEM and fast Fourier transform (inset image) along with the selected area electron diffraction (SAED) pattern for MNP, respectively. On the one hand, in Fig. 2c the microstructure of MNP revealed intense reflection at 2.5 Å, 2.9 Å, and 4.8 Å, which corresponded to the interplanar spacing for (311), (202), and (111) of Fe_3O_4 [30]. On the other hand, Fig. 2d shows the reflection at 2.9 Å, 2.5 Å, and 2.1 Å, which are related to the interplanar spacing for (202), (311), and (400) of Fe_3O_4. These results are consistent with our previous XRD analysis, which shows the presence of Fe_3O_4 as the main phase in our iron oxide MNP.

As stated before, since the XRD patterns of Fe_3O_4 and γ-Fe_2O_3 are very similar, FTIR and Raman spectroscopies were performed to confirm the iron oxide phases present in our MNP (Fig. 3a–b). These vibrational spectroscopies are powerful techniques for distinguishing between iron oxide phases because of their sensitivity to the coordination of the metal-oxide ordering, which directly affects the bond strengths (elastic constants) and vibrations (resonance energies). A typical FTIR spectrum in the 450–850 cm^{-1} range of the MNP is presented in Fig. 3a. The MNP exhibited the typical bands around 450–750 cm^{-1} related to the Fe-O stretching vibration [31,32]. Strong bands at around 600 cm^{-1} were related to the characteristic vibrational mode of Fe-O deformation both in the octahedral and tetrahedral sites of Fe_3O_4 [33,34]. Fig. 3b shows a representative Raman spectrum of the MNP. Predominant contributions related to iron oxide signals were clearly identified. Specifically, strong bands at around 316, 500, and 620 cm^{-1} are characteristic of Fe_3O_4 [35]. Thus, it is clear that the particular features of Fe_3O_4 are predominant in our MNP as the major phase.

To gain a view of the chemical state of the surface of our MNP, XPS was conducted. Fig. 3c–d shows the combined XPS analysis of O 1*s* and Fe 2*p*. Fig. 3c shows the O 1*s* core-level spectra from the MNP. As seen,

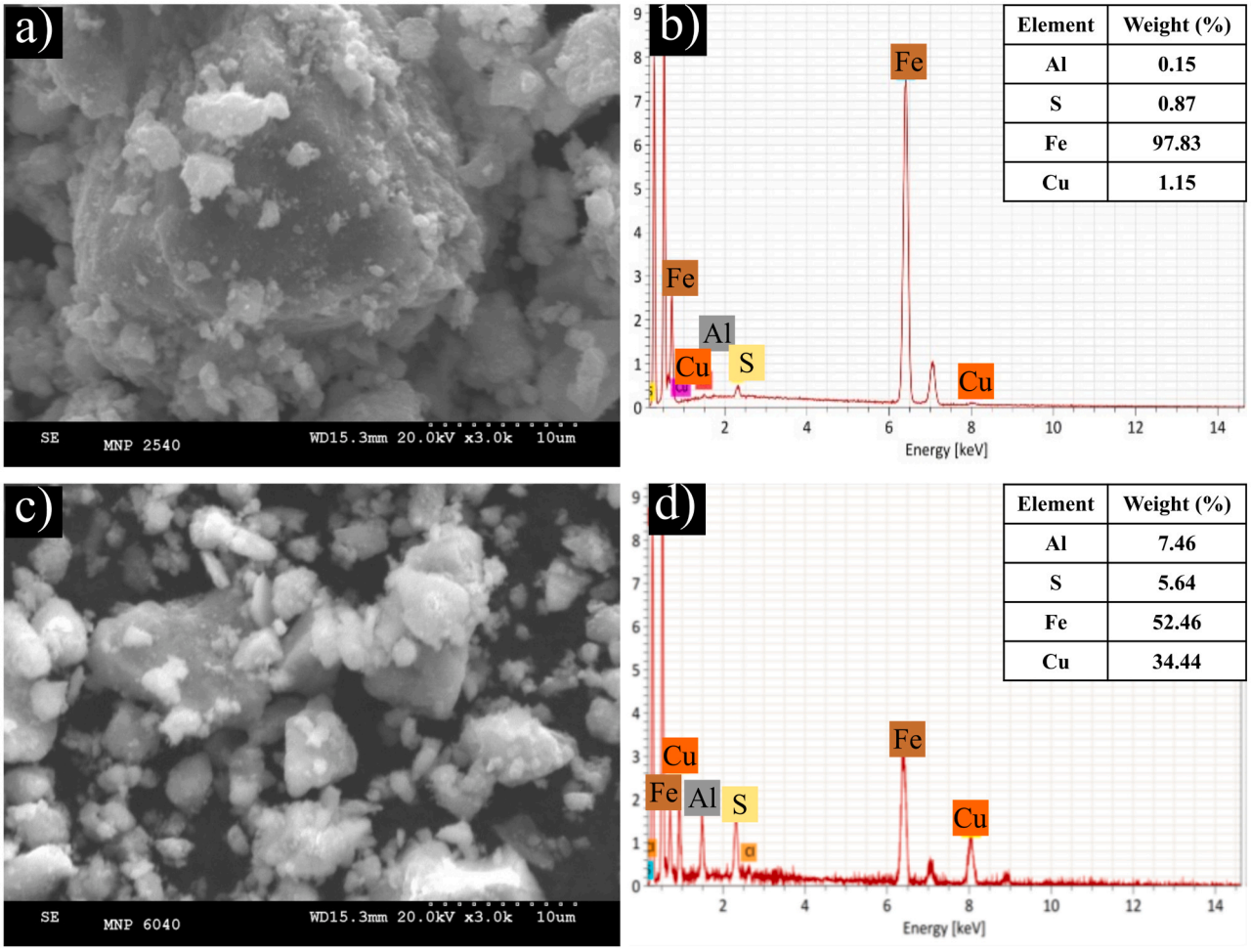

Fig. 5. Representative SEM images and EDX analysis of resultant sludges after the treatment of Cu-rich AMD using MNP at (a–b) pH 2.9 and (c–d) pH 6.0.

the O 1*s* core level exhibited a broad peak, suggesting an additional contribution to the lattice oxygen of the material. In fact, the peak contribution at 529.6 eV is related to the O in the iron oxide lattice (Fe-O). The peak contribution at 530.4 eV is also related to the adsorbed O-H species [36]. In Fig. 3d, the Fe 2*p* core-level spectrum showed two peaks at 724 and 710.4 eV, corresponding to the Fe $2p_{1/2}$ and Fe $2p_{3/2}$ signals, respectively. The experimental value for the spin-orbit splitting between Fe $2p_{1/2}$ and Fe $2p_{3/2}$ resulted in 13.6 eV, suggesting that the surface of our MNP was significantly oxidized. The peak fitting analysis of the Fe $2p_{3/2}$ core-level exhibited two peaks at 710.0 eV and 711.8 eV, which were assigned to the Fe^{3+} and Fe^{2+} valence state [37]. Also, it is important to note the presence of a third signal at 719.0 eV, corresponding to the Fe^{3+} satellite peak of γ-Fe_2O_3, confirming its presence at the surface of our MNP [38,39].

To study the local structure of the MNP synthesized in this study, XANES spectroscopy experiments were performed. XANES spectroscopy has been widely used to study iron oxide [40–42]. Measurements at the Fe K-edge XANES spectra of the MNP and a selected set of references are shown in Fig. S1. The K-edge position was found to be between the Fe^{3+} and Fe^{2+} references. This supports the idea that Fe_3O_4 is the main part of the MNP used in this study. Fig. S2 shows the Mössbauer spectra of MNP at room temperature. The spectra have been fitted as a sum of two sextets corresponding to the Fe tetrahedral and octahedral sites, with the obtained areas similar to those expected for magnetite. Additionally, the MNP exhibited a superparamagnetic nature, as confirmed by VSM characterization (Fig. S3).

3.2. Cu-rich AMD treatment

After the physicochemical characterization of the iron oxide system, it was applied as an adsorbent of metal contaminants present in a Cu-rich AMD. It was decided to apply it in two processes: (i) directly to the Cu-rich AMD (pH 2.9) and (ii) in a two-step treatment, namely, the addition of the MNP followed by a basification (up to pH 6.0). Table 1 shows the chemical composition of the synthetic Cu-rich AMD before and after the direct and the two-step treatment. The results showed that as the Cu-rich AMD is directly treated with the MNP, a significant decrease in the total metal concentration occurred for Cu (20 %), Zn (14 %), Ca (5 %), Co (4 %), Mg (4 %). Interestingly, no significant change was found for Fe total concentration, indicating that no significant Fe dissolution from nanoparticles occurred during the current treatment.

Because the composition of the Cu-rich AMD is a highly saturated medium, we also evaluated the effect of the basification on the total metal concentration (without the presence of MNP). As expected, the total metal concentration significantly decreased after basification for several metal contaminants via precipitation. Basification in the absence of the MNP removed both Fe and Al and decreased Cu (58 %), Zn (34 %), Mg (6 %), and K (4 %). Additionally, no significant change occurred for Ca, Na, and Co. More importantly, the two-step treatment of AMD using a combined approach of MNP and basification evidenced an even greater decrease in the metal concentration for Cu (70 %), Co (13 %), and Mg (10 %), along with no presence of either Fe or Al. It is important to note that the use of MNP confers a distinct advantage over Cu-rich AMD treatment alone, as it not only removes the majority of the metal

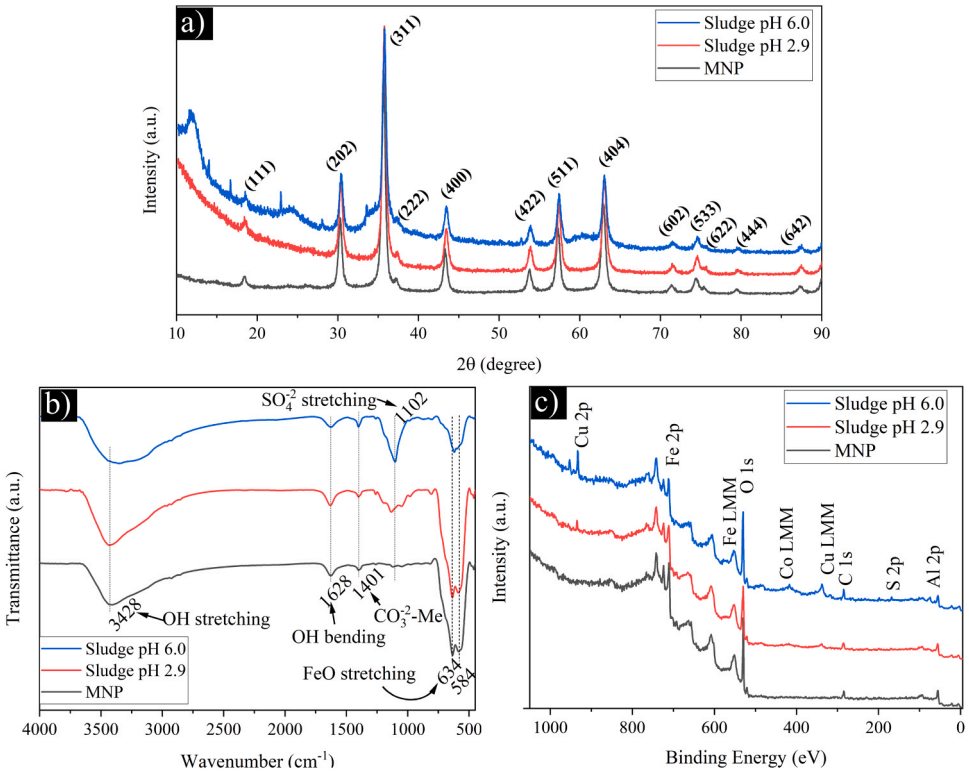

Fig. 6. (a) XRD, (b) FTIR, and (c) survey XPS spectra of the synthesized MNP and its sludge after the Cu-rich AMD treatment.

via precipitation but also significantly improves the separation of the sludge and solution, such as been described for iron oxide nanoparticles applied to the treatment of gold and coal mine AMD [13,43,44].

In order to grasp a better understanding of the Cu adsorption mechanism from AMD onto MNP, kinetic reaction models were used. As shown in Table 2 and Fig. 4, the experimental data for Cu adsorption on MNP at pH 2.9 and 6.0 were fitted with a PSO kinetic model. Based on the data presented in Table 2, the correlation coefficients R^2 for the PSO model were quite good. Additionally, the fitting diagram reflects this finding (Fig. 4). It is essential to highlight that the pronounced elevation of the Cu adsorption curve at pH 6.0 compared to pH 2.9 signifies a substantial contribution of precipitation processes. Thus, these results suggest that during the Cu adsorption process on MNP, the rate of adsorption was influenced by the high concentration of Cu in the solution and the pH.

As SEM-EDX was used to explore the elemental distribution in the solid sludge materials, several metal contaminants from Cu-rich AMD are detected (Fig. 5). Fig. 5a and c show SEM images of sludge's materials at pH 2.9 and 6.0, respectively. In both cases, structures around 10 μm were observed. On the other hand, Fig. 5b and d present the EDX analysis of the contaminant element detected in the sludge materials at pH 2.9 and pH 6.0, respectively. The main elements detected in both sludges were Fe, Cu, S, and Al. In the two-step treatment (sludge at pH 6.0), peaks corresponding to Fe and O decrease significantly in line with the increase in Cu, S, and Al due to the adsorption of metal contaminants on the surface of the MNP.

Fig. 6a shows the XRD patterns of representative sludge samples after the treatment of Cu-rich AMD. As shown in Fig. 6a, the XRD patterns of sludges showed the characteristic diffraction indices of our MNP. This indicates the preservation of the crystal structure of our MNP after the Cu-rich AMD, even at the lower pH, which is consistent with the atomic absorption spectroscopy results. However, it is important to note that the crystalline degree of the MNP slightly decreased after the treatment of the Cu-rich AMD. Likewise, this decrease in the crystallinity became stronger after the two-step treatment due to the huge amount of amorphous material adsorbed onto the MNP surface.

With the aim of characterizing the functional groups of the MNP and the sludges after the Cu-rich AMD treatments, an FTIR study was carried out (Fig. 6b). MNP showed two bands corresponding to the characteristic asymmetric stretching mode of FeO at 538–634 cm^{-1} [34]. For all samples, a band at 1401 cm^{-1} was observed, which corresponds to the characteristic vibration of adsorbed CO_2 on the iron oxides surface of the MNP [45]. After treating Cu-rich AMD with MNP, several specific bands appeared at 950–1200 cm^{-1} related to stretching vibration mode. Four bands at pH 2.9 were observed at 990, 1050, 1133, and 1201 cm^{-1}. The band at 990 cm^{-1} is assigned to the symmetric stretching band (ν1), which becomes IR active when the symmetry is lowered. The other two peaks at 1050 and 1133 cm^{-1} are assigned to the asymmetric stretching (ν3) vibrations [46]. Similar bands have been reported in sulfated metal oxide materials, such as sulfated TiO_2 materials prepared by sol-gel method [47]. On the other hand, at pH 6.0, the intensities of these bands increased after the two-step treatment of Cu-rich AMD and even became a unique intensified one. In this case, the band at 1102 cm^{-1} indicates that sulfate is only bound as outer-sphere complexes [46]. Also, two bands at 1628 cm^{-1} and 3428 cm^{-1} due to the bending mode of water and the stretching mode of adsorbed water, respectively, were detected in all samples. However, the 3428 cm^{-1} band exhibited a broadening for sludge samples. All these results indicate that the metal adsorption mechanism on the MNP depends on the pH. Also, the MNP after the Cu-rich AMD treatments with XPS spectroscopy was analyzed, intending to get an insight into the surface composition. Fig. 6c compares the XPS survey spectra of the MNP and the sludges resultant after the treatment at pH 2.9 and the two-step counterpart at pH 6.0. For all samples, the predominant signals were O 1*s* and Fe 2*p*, centered at about 530 eV and 710 eV, respectively, due to the inherent chemical nature of the MNP [39]. However, after the Cu-rich AMD treatment, the sludges showed interesting changes. First, the sludge at pH 2.9 exhibited a weak signal corresponding to the Cu 2*p* (933 eV), indicating the adsorption of Cu. Second, after the two-step treatment of the Cu-rich AMD, several signals corresponding to Cu 2*p* (933 eV), S 2p (164 eV), Al 2p (74 eV),

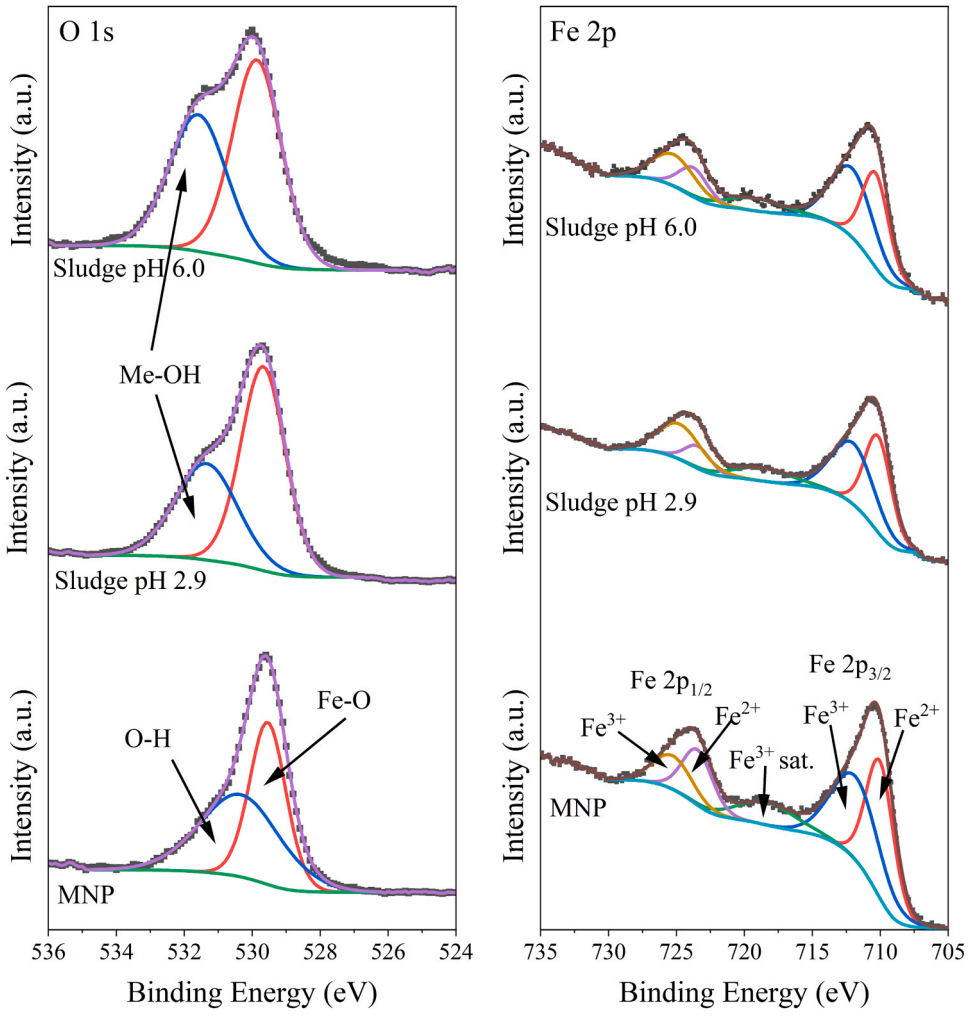

Fig. 7. High-resolution O 1*s* and Fe 2*p* XPS spectra of the synthesized MNP and its sludge after the Cu-rich AMD treatment. Me stands for metal.

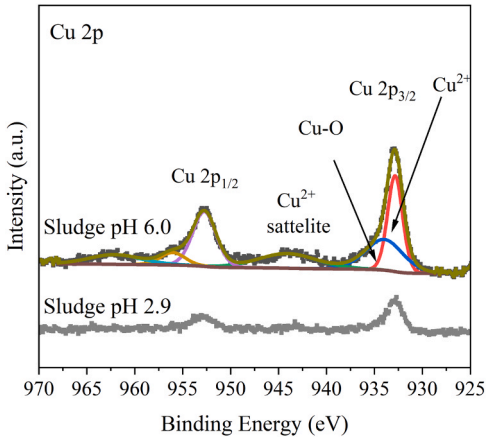

Fig. 8. High-resolution Cu 2*p* XPS spectra of the sludge after the Cu-rich AMD treatment.

and Co 2p (780 eV) appeared, confirming that the adsorption of these metal contaminants present in the Cu-rich AMD solution takes place on the surfaces of the MNP. These results align with the analytical results obtained from the chemical analysis of the solution after the two-step treatment.

To visualize the chemical state of the MNP after the Cu-rich AMD treatment, the high-resolution spectra in the region of Fe 2*p*, O 1*s*, and Cu 2*p* in the corresponding sludge samples were analyzed. Fig. 7 compares the chemical state of O 1*s* and Fe 2*p* core level spectra between the MNP composite and its sludges after the Cu-rich AMD treatment at different pH. Fig. 7a shows the peak fitting for the O 1*s* core-level spectra. Two peaks at 529.9 eV and 531.6 eV were related to species adsorbed onto the surface of Fe-O and O-H, respectively [36]. Remarkably, in both sludges of pH 2.9 and 6.0, the oxygen peak shifted toward higher energies. However, the change is more evident in the sludge of pH 6.0 due to the large amount of metallic cations adsorbed onto the MNP surface [48]. In Fig. 7b the Fe $2p_{3/2}$ exhibits two peaks at 710.3 eV and 712.0 eV assigned to the Fe^{3+} and Fe^{2+} valence states [37]. Interestingly, after the Cu-rich AMD treatment, the proportion of these contributions changes compared to the pristine MNP. In fact, there was an increase in the Fe^{3+} contribution due to surface oxidation that increased with the basification. Also, the spin-orbit coupling changes slightly from 13.6 eV to 13.7 eV.

Fig. 8 shows the Cu 2*p* core level spectra of the representative sludge samples. The Cu 2*p* exhibited the typical double peak at 952.8 eV and 932.9 eV, corresponding to the (Cu $2p_{1/2}$) and (Cu $2p_{3/2}$) signals, respectively. First, it is worth mentioning that the signal of Cu 2*p* significantly increased in the sludge with a pH of 6.0 compared to the sludge with a pH of 2.9. Also, due to the low intensity in the Cu 2*p* signal of the sludge of pH 2.9, we only performed a peak fitting analysis in the sample of sludge of pH 6.0. Thus, the determination of the chemical state by peak fitting analysis of Cu $2p_{3/2}$ indicated two characteristic

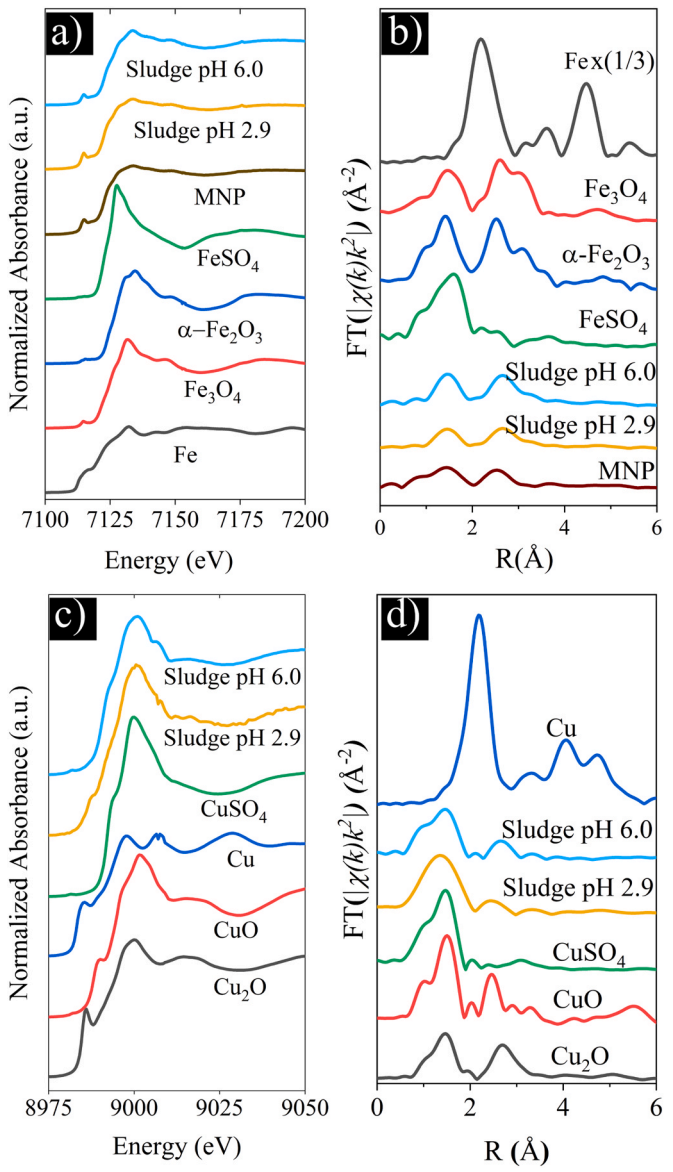

Fig. 9. XANES and radial distribution functions from EXAFS spectra for (a and b) Fe and (c and d) Cu spectra from the synthesized MNP and its sludge after the Cu-rich AMD treatment. The abbreviation "FT" stands for Fourier Transform.

contributions at about 932.8 eV corresponding to Cu^{2+} and 934.1 eV related to Cu-O [49]. It is important to mention that there was no evidence of Cu^{2+} reduction into Cu^0. Previously, the reduction of this metal has been documented during the study of nanoscale zerovalent iron (nZVI) for the specific creation of Cu nanoparticles from AMD. The authors verified the presence of nanoparticles containing metallic copper (Cu^0) using XPS. The process of Cu removal was determined to be most likely by cementation with metallic iron (Fe^0) [50].

XANES spectra Fe K-edge and pre-edge for MNP and its sludge after the two-step treatment are shown in Fig. 9a. The common features observed in the spectra of the MNP and its sludges suggested that Fe_3O_4 was the main iron oxide phase, as indicated by the previous characterizations. Table S2 summarizes the position of the edges and their relative displacement from the metallic state position. Kunzl's law states that the displacements of the edge position are associated with changes in the oxidation state, providing a reasonable estimation of the oxidation state in many compounds [51]. Therefore, the valence can be linearly fitted against the edge position. Following Kunzl's proportionality, the iron oxidation state for MNP was $Fe^{+2.4}$ while the sludge of pH 2.9 and the sludge of pH 6.0 were $Fe^{+2.4}$ and $Fe^{+2.6}$, respectively. These results suggest that the acid pH solution does not significantly affect the average iron oxidation state. On the other hand, the oxidation state increased after the basification process. Fig. 9b shows the Fourier transform (FT) of the EXAFS signal for MNP and its sludge after the two-step treatment. As the figure shows, the EXAFS also pointed out that magnetite is the main component in the sludges. The higher intensity of the FT in the sludge of pH 6.0 suggested a more defined phase composition driven by the basification process.

Additional information on the Cu speciation in the MNP surface is provided by analyzing the Cu K-edge. Fig. 9c shows the Cu K-edge spectra of the MNP and its sludge after the two-step treatment. Spectra from the sludge samples shared the main features with the spectrum of the $CuSO_4$ and Cu oxides. However, the prominence of a second resonance after the main peak coincided with the one presented in the metallic Cu spectrum. By performing a semiquantitative estimation of the phase composition by least-square fitting with the main references [52,53] (Fig. S4), it is observed that in the sludge of pH 2.9 Cu is adsorbed on the surface as a combination of CuO (29 %) and $CuSO_4$ (71 %). At the sludge of pH 6.0, the Cu is adsorbed in a larger relative composition in $CuSO_4$ (56 %) and Cu_2O (20 %) plus CuO (24 %). The Cu relative composition agreed with the average oxidation state estimated by the edge position spectra, Cu^{+2} in the sludge of pH 2.9 and $Cu^{+2.4}$ in the sludge of pH 6.0 (see Table S2). The local structure of Cu determined by EXAFS (Fig. 9d) shows a coordination shell close to the one corresponding to $CuSO_4$ and main oxides (CuO, Cu_2O) in the real space.

3.3. DFT calculations and adsorption mechanism

We conducted first-principles calculations using DFT theory to enhance the understanding of how different Cu ion species adsorb to the surface of Fe_3O_4 according to the pH of Cu-rich AMD. According to previous experimental results, when iron oxides are immersed in an aqueous solution, they acquire surface groups such as -FeOH, among others [54]. Under conditions where the pH value was either above or below the isoelectric point, protonation or deprotonation leads to the conversion of hydroxyl groups of -FeOH on the surface into functional groups of $FeOH_2^+$ or FeO^- [55]. Thus, the equilibrium between protonation and deprotonation occurs at the isoelectric point of Fe_3O_4 and is dependent on the solution pH [56]. For that reason, in the present study, the optimized Fe_3O_4 bulk was used to build the (001) surface structure with two different terminations (-FeOH and -FeO were used to simulate pH 2.9 and pH 6.0 of Cu-rich AMD, respectively) to simulate the effect of pH on the surface chemistry of the MNP in aqueous solution (Fig. S5). Also, earlier research has shown that Cu^{2+}, $Cu(OH)^+$ and $Cu(OH)_2$ (which can precipitate; see discussion of Figure S6) are the main types of Cu ions found in water below pH 7, with Cu^{2+} being the main type of chemical at lower pH levels [57]. For that reason, we considered these Cu ion species in our simulations. Fig. 10 shows the optimized Cu^{2+} and $Cu(OH)^+$ ion onto the Fe_3O_4 (001) surface models. It is interesting to note that the adsorption of both types of Cu species was thermodynamically favorable in the different Fe_3O_4 (001) termination surface models. However, significant differences exist in the adsorption energies onto the -FeOH and -FeO termination surfaces. On the one hand, the calculated adsorption energy of Cu^{2+} on the surface of -FeOH termination was − 0.94 eV. On the contrary, the calculated adsorption energies of Cu^{2+} and $Cu(OH)^+$ on the surface of the -FeO termination were − 4.40 eV and − 3.12 eV, respectively, which is significantly lower than the -FeOH surface. Likewise, the adsorption energy of $Cu(OH)_2$ on the surface of the -FeO termination of the Fe_3O_4 was − 3.63 eV (Fig. S6). These results indicate that the adsorption of Cu species onto the -FeO surfaces (simulating pH 6.0) is thermodynamically more stable than on the -FeOH surface (simulating pH 2.9). As shown in Fig. 10a–f, it is evident that Cu species exhibit various adsorption sites on the surface. On the one hand, the Cu^{2+} interacts mostly with O atoms in the -FeO

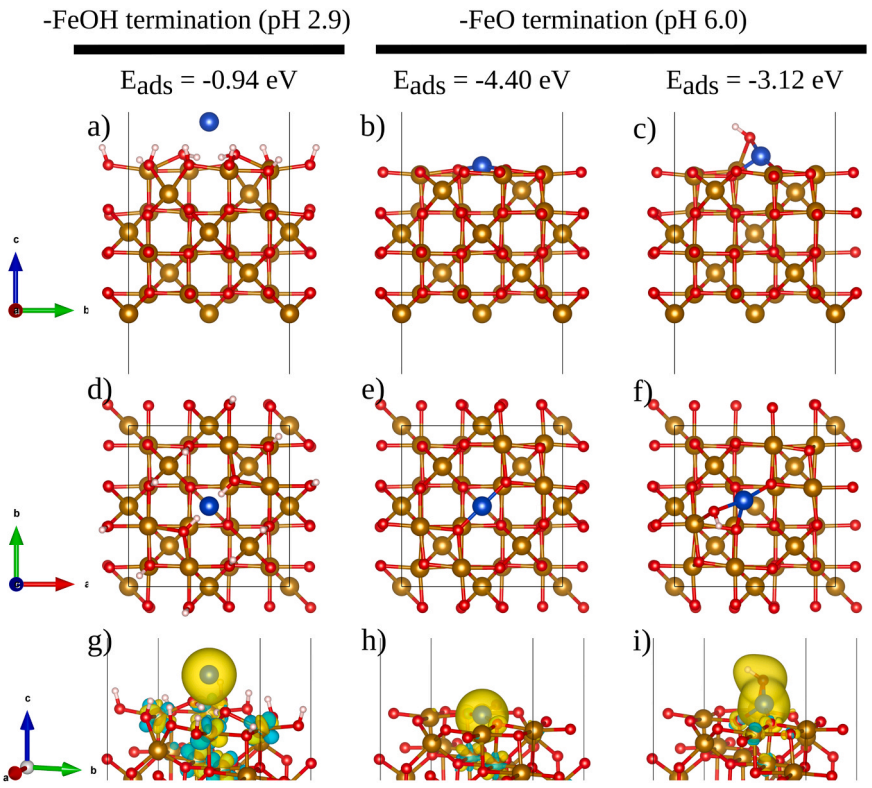

Fig. 10. Optimized adsorption and CDD of Cu ion species on the Fe_3O_4 (001) surface models used in the present study (a–c side views and d–f top views). For the -FeOH termination surface models, only Cu^{2+} is optimized (a, d, and g), while for the -FeO termination surface model, both Cu^{2+} (b, e, and h) and $Cu(OH)^{+}$ (c, f, and I) have been optimized. Fe, Cu, O, and H atoms are represented by brown, blue, red, and white balls, respectively.

surface termination, creating Cu–O complexes. On the other hand, at the -FeOH surface the H atoms prevent the formation of Cu–O complexes. $Cu(OH)^{+}$ interacts primarily with the O atom of –OH and forms Cu–O–Fe complexes by combining with Fe atoms, as described previously for specularite, a α–Fe_2O_3-based iron oxide mineral [58]. Additionally, the adsorption energies for the other metallic chemical species (M^{n+}) found in our Cu-rich AMD can be seen in Table S3. To further explore the correlation between Cu ion species and the Fe_3O_4 (001) surface, Fig. 10g–i displays the electron density around adsorbed Cu^{2+} and $Cu(OH)^{+}$ ions. Here, as the color changes from yellow to green, the atoms gradually lose their ability to absorb electrons. As can be appreciated in Fig. 10g–h, there was an increase in electron density around the Cu^{2+} for both, while O atoms interacting with Cu^{2+} decreased their electron density. However, on the -FeOH terminating surface, the presence of H atoms passivated the variation of the electron density coming from O atoms. The situation was more complicated for the adsorption of $Cu(OH)^{+}$.

Fig. 11a–b shows the partial density of states (pDOS) for the atoms at a Fe_3O_4 (001) slab model and the adsorbed Cu^{2+} ion around the Fermi Energy (E_F). In general, the pDOS for the -FeOH termination exhibited high-intensity localized Cu d states. On the contrary, the pDOS for the -FeO termination showed wide Cu 3d states hybridization with O 2p states, indicating the formation of Cu–O complexes.

Taking together, according to the results described in the present study, the treatment of Cu-rich AMD with the use of MNP exhibits significant removal of metal contaminants (Cu, Co, Zn, Fe, and Al). Enhanced efficiency is observed through a two-step treatment involving both MNP addition and basification. It is important to mention that adsorption of heavy metal ions onto nanoadsorbents has been described via various mechanisms, such as physical adsorption, chemisorption, electrostatic interactions, simple diffusion, intra-particle diffusion, hydrogen bonding, redox interactions, complexation, ion exchange, precipitation, and pore adsorption [59]. The results of our research indicate that the adsorption kinetics can be described by a pseudo-second-order model. Moreover, a physical adsorption process at pH 2.9 and a combined precipitation/chemical adsorption process at pH 6.0 were determined. Although numerous reports have discussed the use of iron oxides for remediating heavy metals from wastewaters [60–63], the removal mechanisms related to iron oxide nanoparticles are the subject of apparent inconsistencies in the scientific literature [64]. Several research studies propose that the mechanism at the atomistic level involves physisorption or van der Waals interactions [65]. Conversely, others describe chemical reactions involving functional groups known as chemisorption [66,67]. In our case, DFT calculations reveal that the adsorption mechanism is pH-dependent, with stronger Cu-O bond formation occurring at higher pH levels. Thus, it is important to remark that the operational mechanism is contingent on the pH level of the solution. At pH 2.9, all metals are in their cation form (for example as Cu^{2+}) and the Fe_3O_4 (001) termination is protonated. The cations can adsorb with the hydroxylated-terminated sites of the MNP, involving the formation of van der Waals interactions as a physisorption process:

$$Cu^{2+} + Bulk - FeOH \Leftrightarrow Bulk - FeOH - Cu \quad (4)$$

where $Bulk - FeOH$ represents the surface of the MNP and $Bulk - FeOH - Cu$ represents the Cu^{2+} physisorbed onto the surface of the MNP. Consequently, at this pH level, the adsorption of Cu^{2+} on the Fe_3O_4 (001) surface at pH 2.9 is weak (– 0.94 eV).

On the contrary, when the pH level is 6.0, metals exist in a mixture of cations, and cation-hydroxide forms due to basification, while oxyhydroxide precipitates can also occur (here simplified by $Cu(OH)_2$; see Fig. S6). Likewise, at this pH level, the Fe_3O_4 (001) termination is deprotonated. The metal species can react with the O-terminated sites of the MNP, involving the formation of cation-oxygen bonds represented by the complexation surface reactions:

$$Cu^{2+} + Bulk - FeO \rightarrow Bulk - FeO - Cu \quad (5)$$

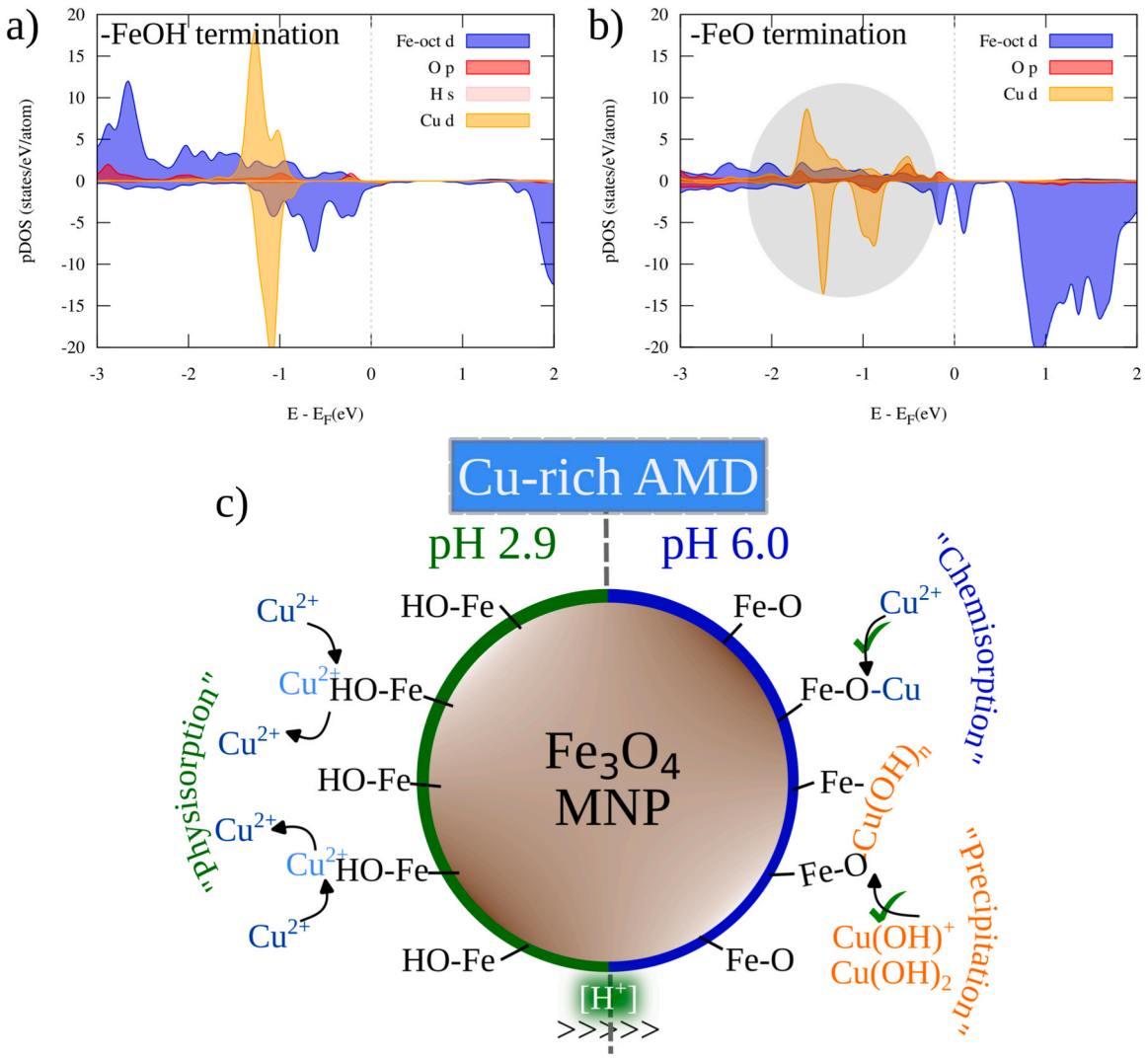

Fig. 11. Partial density of states (pDOS) for Cu^{2+} adsorption on the (a) -FeOH and (b) -FeO terminations of Fe_3O_4 (001) surface models. (c) Schematic representation of the adsorption mechanism of Cu species from Cu-rich AMD on MNP.

$$Cu(OH)^{+} + Bulk - FeO \rightarrow Bulk - FeO - Cu + OH^{-} \quad (6)$$

where $Bulk - FeO$ and $Bulk - FeO - Cu$ represent the O-terminated sites of the MNP and the Cu adsorbed to it, respectively. In this case, the adsorption of Cu^{2+}, $Cu(OH)^{+}$ and $Cu(OH)_2$ on the surface of Fe_3O_4 (001) at pH 6.0 is strong (− 4.40 eV, − 3.12 eV and − 3.63 eV), resulting in the formation of chemical bonds between the adsorbate and the adsorbent and involving both chemisorption and precipitation processes.

4. Conclusions

In the present study, a MNP has been synthesized by the co-precipitation method and further applied in the treatment of Cu-rich AMD at different pH values. The resulting MNP and the respective sludge samples after the Cu-rich AMD treatment were characterized in terms of crystal structure, physical properties, morphology, size, and chemical composition. The experimental results showed that the MNP exhibited excellent adsorption capacity for Cu ions in the AMD, even at acid pH. We identified the chemical species adsorbed onto the MNP, the oxidation state of the resultant sludge after the Cu-rich AMD treatment, and the short-range ordering of metal contaminant species on the surface of the MNP. Furthermore, DFT calculations were performed to gain insights into the underlying mechanism of Cu adsorption onto the iron oxide MNP. The adsorption mechanism between MNP and Cu species is primarily attributed to metal cation-oxygen bond surface complexation at pH 6.0 and physisorption at pH 2.9. To sum up, this experimental and theoretical investigation of the treatment of Cu-rich AMD using iron oxide MNP has provided valuable insights into the adsorption behavior and mechanisms involved in removing Cu ions from AMD. This information will help to solve the adsorption mechanism of metal contaminants onto the surface of the MNP, thus allowing us to engineer them more specifically.

CRediT authorship contribution statement

Teófilo Graber: Writing – review & editing, Validation, Supervision, Project administration, Funding acquisition. **Jorge Jorge Sánchez-Marcos:** Writing – review & editing, Methodology, Investigation, Formal analysis, Data curation. **Fernando Agulló-Rueda:** Writing – review & editing, Validation, Methodology, Investigation. **Nelson Naveas:** Writing – review & editing, Writing – original draft, Visualization, Supervision, Software, Resources, Project administration, Methodology, Investigation, Funding acquisition, Formal analysis, Data curation, Conceptualization. **Miguel García:** Writing – review & editing, Methodology, Investigation. **Ruth Pulido:** Writing – review & editing, Writing – original draft, Visualization, Validation, Methodology, Investigation, Formal analysis, Data curation, Conceptualization.

Miguel Manso-Silvan: Writing – review & editing, Visualization, Validation, Supervision, Software, Resources, Project administration, Methodology, Funding acquisition, Conceptualization. **Carlo Marini:** Writing – review & editing, Investigation, Formal analysis, Data curation. **Leonardo Soriano:** Writing – review & editing, Supervision, Methodology, Investigation. **Jacobo Hernández-Montelongo:** Writing – review & editing, Visualization, Validation, Methodology, Investigation. **Álvaro Muñoz-Noval:** Writing – review & editing, Investigation, Formal analysis, Data curation. **María Sevilla:** Writing – review & editing, Visualization, Validation, Methodology, Investigation. **Raúl Martín-Palma:** Writing – review & editing, Validation, Supervision, Investigation, Funding acquisition. **Iván Brito:** Writing – review & editing, Validation, Methodology, Investigation.

Declaration of Competing Interest

The authors declare that they have no known competing financial interests or personal relationships that could have appeared to influence the work reported in this paper.

Data availability

Data will be made available on request.

Acknowledgements

The CONICYT PFCHA/DOCTORADO/2017-21172001 (Nelson Naveas) provided financial support for this work. M.M.S acknowledges funding from MCIN/AEI/10.13039/501100011033 (PID2020-112770RB-C22). The authors thank the PhD programs in -"Advanced Materials and Nanotechnology" from Universidad Autónoma de Madrid (UAM, Spain) and "Ingeniería de Procesos de Minerales" from Universidad de Antofagasta (UA, Chile). The simulations used in this paper have been performed in the Centro de Computación Científica-Universidad Autónoma de Madrid (CCC-UAM); thanks to CPU time and other resources granted by the institution.

Appendix A. Supporting information

Supplementary data associated with this article can be found in the online version at doi:10.1016/j.jece.2024.113822.

References

[1] B. Rezaie, A. Anderson, Sustainable resolutions for environmental threat of the acid mine drainage, Sci. Total Environ. 717 (2020) 137211.
[2] H.M. Anawar, Sustainable rehabilitation of mining waste and acid mine drainage using geochemistry, mine type, mineralogy, texture, ore extraction and climate knowledge, J. Environ. Manag. 158 (2015) 111–121.
[3] L. Tong, R. Fan, S. Yang, C. Li, Development and status of the treatment technology for acid mine drainage, Min. Metall. Explor. 38 (2020) 1–13.
[4] D. Blowes, C. Ptacek, J. Jambor, C. Weisener, D. Paktunc, W. Gould, D. Johnson, 11.5 – the geochemistry of acid mine drainage, in: H.D. Holland, K.K. Turekian (Eds.), Treatise on Geochemistry, Second ed., Elsevier, Oxford, 2014, pp. 131–190. ⟨https://www.sciencedirect.com/science/article/pii/B9780080959757009050⟩, 10.1016/B978-0-08-095975-7.00905-0.
[5] E.-T. Tolonen, A. Sarpola, T. Hu, J. Rämö, U. Lassi, Acid mine drainage treatment using by-products from quicklime manufacturing as neutralization chemicals, Chemosphere 117 (2014) 419–424.
[6] M. Zhang, H. Wang, X. Han, Preparation of metal-resistant immobilized sulfate reducing bacteria beads for acid mine drainage treatment, Chemosphere 154 (2016) 215–223.
[7] B. VaziriHassas, M. Rezaee, S.V. Pisupati, Precipitation of rare earth elements from acid mine drainage by CO_2 mineralization process, Chem. Eng. J. 399 (2020) 125716.
[8] J. SánchezEspaña, E. Santofimia Pastor, E. López Pamo, Iron terraces in acid mine drainage systems: a discussion about the organic and inorganic factors involved in their formation through observations from the Tintillo acidic river (Riotinto mine, Huelva, Spain), Geosphere 3 (2007) 133–151.
[9] K. Ambiado, C. Bustos, A. Schwarz, R. Bórquez, Membrane technology applied to acid mine drainage from copper mining, Water Sci. Technol. 75 (2016) 705–715.
[10] Y. Song, Z. Guo, R. Wang, L. Yang, Y. Cao, H. Wang, A novel approach for treating acid mine drainage by forming schwertmannite driven by a combination of biooxidation and electroreduction before lime neutralization, Water Res. 221 (2022) 118748.
[11] I.L.-H.L.A.C.-S.G.S. C. Romel González-Hernández, V. Martínez-Miranda, R. Cortés-Martínez, Acid mine drainage (amd) treatment using galvanic electrochemical system Al-Cu, Environ. Technol. 44 (2023) 4424–4440 (PMID: 35731670).
[12] F. Pagnanelli, I. De Michelis, S. DiMuzio, F. Ferella, F. Veglió, Bioassessment of a combined chemical-biological treatment for synthetic acid mine drainage, J. Hazard. Mater. 159 (2008) 567–573.
[13] K.K. Kefeni, B.B. Mamba, T.A. Msagati, Magnetite and cobalt ferrite nanoparticles used as seeds for acid mine drainage treatment, J. Hazard. Mater. 333 (2017) 308–318.
[14] A. Atrei, M. Fiorani, A. Bellingeri, G. Protano, I. Corsi, Remediation of acid mine drainage-affected stream waters by means of eco-friendly magnetic hydrogels crosslinked with functionalized magnetite nanoparticles, Environ. Nanotechnol. Monit. Manag. 12 (2019) 100263.
[15] S. Dubey, S. Banerjee, S.N. Upadhyay, Y.C. Sharma, Application of common nanomaterials for removal of selected metallic species from water and wastewaters: a critical review, J. Mol. Liq. 240 (2017) 656–677.
[16] S. Tang, I. Lo, Magnetic nanoparticles: essential factors for sustainable environmental applications, Water Res. 47 (2013).
[17] M. Torregrosa, A. Schwarz, I. Nancucheo, E. Balladares, Evaluation of the bio-protection mechanism in diffusive exchange permeable reactive barriers for the treatment of acid mine drainage, Sci. Total Environ. 655 (2019) 374–383.
[18] P. Giannozzi, S. Baroni, N. Bonini, M. Calandra, R. Car, C. Cavazzoni, D. Ceresoli, G.L. Chiarotti, M. Cococcioni, I. Dabo, A.D. Corso, S. de Gironcoli, S. Fabris, G. Fratesi, R. Gebauer, U. Gerstmann, C. Gougoussis, A. Kokalj, M. Lazzeri, L. Martin-Samos, N. Marzari, F. Mauri, R. Mazzarello, S. Paolini, A. Pasquarello, L. Paulatto, C. Sbraccia, S. Scandolo, G. Sclauzero, A.P. Seitsonen, A. Smogunov, P. Umari, R.M. Wentzcovitch, Quantum espresso: a modular and open-source software project for quantum simulations of materials, J. Phys.: Condens. Matter 21 (2009) 395502.
[19] G. Prandini, A. Marrazzo, I.E. Castelli, N. Mounet, N. Marzari, Precision and efficiency in solid-state pseudopotential calculations, npj Comput. Mater. 4 (2018).
[20] A. Dal Corso, Pseudopotentials periodic table: from H to Pu, Comput. Mater. Sci. 95 (2014) 337–350.
[21] N. Naveas, R. Pulido, C. Marini, J. Hernández-Montelongo, M.M. Silván, First-principles calculations of hematite (α -Fe_2O_3) by self-consistent DFT + U + V, iScience 26 (2023) 106033.
[22] N. Naveas, R. Pulido, C. Marini, P. Gargiani, J. Hernandez-Montelongo, I. Brito, M. Manso-Silván, First-principles calculations of magnetite (Fe_3O_4) above the verwey temperature by using self-consistent DFT + U + V, J. Chem. Theory Comput. 19 (2023) 8610–8623 (PMID: 37974305).
[23] M. Cococcioni, S. de Gironcoli, Linear response approach to the calculation of the effective interaction parameters in the LDA + U method, Phys. Rev. B 71 (2005) 035105.
[24] R. Pentcheva, F. Wendler, H.L. Meyerheim, W. Moritz, N. Jedrecy, M. Scheffler, Jahn-Teller stabilization of a "polar" metal oxide surface: Fe_3O_4(001), Phys. Rev. Lett. 94 (2005) 126101.
[25] N. Mulakaluri, R. Pentcheva, M. Wieland, W. Moritz, M. Scheffler, Partial dissociation of water on Fe_3O_4(001): adsorbate induced charge and orbital order, Phys. Rev. Lett. 103 (2009) 176102.
[26] P. Xue, Z. Fu, X. Chu, Y. Zhang, Z. Yang, Density functional theory study on the interaction of co with the Fe3O4(001) surface, Appl. Surf. Sci. 317 (2014) 752–759.
[27] C. Haavik, S. Stølen, H. Fjellvåg, M. Hanfland, D. Häusermann, Equation of state of magnetite and its high-pressure modification: thermodynamics of the Fe-O system at high pressure, Am. Mineral. 85 (2000) 514–523.
[28] C. Pecharromán, T. González-Carreño, J. Iglesias, The infrared dielectric properties of maghemite, γ -Fe_2O_3, from reflectance measurement on pressed powders, Phys. Chem. Miner. 22 (1995) 21–29.
[29] W. Kim, C.-Y. Suh, S.-W. Cho, K.-M. Roh, H. Kwon, K. Song, I.-J. Shon, A new method for the identification and quantification of magnetite-maghemite mixture using conventional x-ray diffraction technique, Talanta 94 (2012) 348–352.
[30] P. Tipsawat, U. Wongpratat, S. Phumying, N. Chanlek, K. Chokprasombat, S. Maensiri, Magnetite (Fe_3O_4) nanoparticles: synthesis, characterization and electrochemical properties, Appl. Surf. Sci. 446 (2018) 287–292 (12th International Conference on Surfaces, Coatings and Nanostructured Materials - NANOSMAT 2017).
[31] B. Pandey, A. Shahi, J. Shah, R. Kotnala, R. Gopal, Optical and magnetic properties of Fe_2O_3 nanoparticles synthesized by laser ablation/fragmentation technique in different liquid media, Appl. Surf. Sci. 289 (2014) 462–471.
[32] R.A. Ismail, G.M. Sulaiman, S.A. Abdulrahman, T.R. Marzoog, Antibacterial activity of magnetic iron oxide nanoparticles synthesized by laser ablation in liquid, Mater. Sci. Eng.: C 53 (2015) 286–297.
[33] V. Svetlichnyi, A. Shabalina, I. Lapin, D. Goncharova, D. Velikanov, A. Sokolov, Characterization and magnetic properties study for magnetite nanoparticles obtained by pulsed laser ablation in water, Appl. Phys. A 123 (2017).
[34] V.A. Svetlichnyi, A.V. Shabalina, I.N. Lapin, D.A. Goncharova, D.A. Velikanov, A. E. Sokolov, Study of iron oxide magnetic nanoparticles obtained via pulsed laser ablation of iron in air, Appl. Surf. Sci. 462 (2018) 226–236.
[35] D.L.A. de Faria, S. VenâncioSilva, M.T. de Oliveira, Raman microspectroscopy of some iron oxides and oxyhydroxides, J. Raman Spectrosc. 28 (1997) 873–878.

[36] M. Aronniemi, J. Sainio, J. Lahtinen, XPS study on the correlation between chemical state and oxygen-sensing properties of an iron oxide thin film, Appl. Surf. Sci. 253 (2007) 9476–9482.
[37] T. Radu, C. Iacovita, D. Benea, R. Turcu, X-ray photoelectron spectroscopic characterization of iron oxide nanoparticles, Appl. Surf. Sci. 405 (2017) 337–343.
[38] J.A. Cuenca, K. Bugler, S. Taylor, D. Morgan, P. Williams, J. Bauer, A. Porch, Study of the magnetite to maghemite transition using microwave permittivity and permeability measurements, J. Phys.: Condens. Matter 28 (2016) 106002.
[39] A. Grosvenor, B. Kobe, M. Biesinger, N. Mcintyre, Investigation of multiplet splitting of Fe 2p XPS spectra and bonding in iron compounds, Surf. Interface Anal. 36 (2004) 1564–1574.
[40] C. Piquer, M. Laguna-Marco, A.G. Roca, R. Boada, C. Guglieri, J. Chaboy, Fe K-edge x-ray absorption spectroscopy study of nanosized nominal magnetite, J. Phys. Chem. C 118 (2014) 1332–1346.
[41] M. Soldatov, J. Goettlicher, S. Kubrin, A. Guda, T. Lastovina, A. Bugaev, Y. Rusalev, A. Soldatov, C. Lamberti, The insight from x-ray absorption spectroscopy to octahedral/tetrahedral site distribution in Sm-doped iron oxide magnetic nanoparticles, J. Phys. Chem. C 122 (2018).
[42] N. Finck, L. Radulescu, D. Schild, M. Rothmeier, F. Huber, J. Lützenkirchen, T. Rabung, F. Heberling, M. Schlegel, K. Dideriksen, S. Nedel, H. Geckeis, XAS signatures of Am(III) adsorbed onto magnetite and maghemite, J. Phys.: Conf. Ser. 712 (2016) 012085.
[43] K.K. Kefeni, T.M. Msagati, B.B. Mamba, Synthesis and characterization of magnetic nanoparticles and study their removal capacity of metals from acid mine drainage, Chem. Eng. J. 276 (2015) 222–231.
[44] K.K. Kefeni, T.A. Msagati, T.T. Nkambule, B.B. Mamba, Synthesis and application of hematite nanoparticles for acid mine drainage treatment, J. Environ. Chem. Eng. 6 (2018) 1865–1874.
[45] F. Mirabella, E. Zaki, F. IvarsBarceló, S. Schauermann, S. Shaikhutdinov, H.-J. Freund, CO_2 adsorption on magnetite Fe_3O_4 (111), J. Phys. Chem. C 122 (2018).
[46] P. Roonasi, A. Holmgren, An ATR-FTIR study of sulphate sorption on magnetite; rate of adsorption, surface speciation, and effect of calcium ions, J. Colloid Interface Sci. 333 (2009) 27–32.
[47] L.K. Noda, R.M. de Almeida, L.F.D. Probst, N.S. Gonçalves, Characterization of sulfated TiO_2 prepared by the sol-gel method and its catalytic activity in the n-hexane isomerization reaction, J. Mol. Catal. A: Chem. 225 (2005) 39–46.
[48] T. Liu, X. Li, T. Waite, Depassivation of aged Fe^0 by divalent cations: correlation between contaminant degradation and surface complexation constants, Environ. Sci. Technol. 48 (2014) 14564–14571.
[49] M.C. Biesinger, Advanced analysis of copper x-ray photoelectron spectra, Surf. Interface Anal. 49 (2017) 1325–1334.
[50] R. Crane, D. Sapsford, Selective formation of copper nanoparticles from acid mine drainage using nanoscale zerovalent iron particles, J. Hazard. Mater. 347 (2018) 252–265.
[51] V. Kunzl, A linear dependence of energy levels on the valency of elements, Collect. Czechoslov. Chem. Commun. 4 (1932) 213–224.
[52] G.P. Huffman, N. Shah, F.E. Huggins, L.M. Stock, K. Chatterjee, J.J. Kilbane, M.-I. M. Chou, D.H. Buchanan, Sulfur speciation of desulfurized coals by Xanes spectroscopy, Fuel 74 (1995) 549–555.
[53] E.M. Saurette, Y.Z. Frinfrock, B. Verbuyst, D.W. Blowes, J.M. McBeth, C.J. Ptacek, Improved precision in As speciation analysis with HERFD-XANES at the As *K*-edge: the case of As speciation in mine waste, J. Synchrotron Radiat. 29 (2022) 1198–1208.
[54] M. Ahmed, S. Ali, S. El-Dek, A. Galal, Magnetite-hematite nanoparticles prepared by green methods for heavy metal ions removal from water, Mater. Sci. Eng.: B 178 (2013) 744–751.
[55] S.R. Chowdhury, E.K. Yanful, A.R. Pratt, Chemical states in XPS and Raman analysis during removal of Cr(VI) from contaminated water by mixed maghemite-magnetite nanoparticles, J. Hazard. Mater. 235–236 (2012) 246–256.
[56] J. Zhang, S. Lin, M. Han, Q. Su, L. Xia, Z. Hui, Adsorption properties of magnetic magnetite nanoparticle for coexistent Cr(VI) and Cu(II) in mixed solution, Water 12 (2020).
[57] J.D. Cuppett, S.E. Duncan, A.M. Dietrich, Evaluation of copper speciation and water quality factors that affect aqueous copper tasting response, Chem. Senses 31 (2006) 689–697.
[58] M. Huangfu, J. Li, X. Zhang, Y. Hu, J. Deng, Y. Wang, P. Wei, Study of the effect of absorbed Cu species on the surface of specularite (0 0 1) by the DFT calculations, Minerals 11 (2021).
[59] Z. Raji, A. Karim, A. Karam, S. Khalloufi, Adsorption of heavy metals: mechanisms, kinetics, and applications of various adsorbents in wastewater remediation—a review, Waste 1 (2023) 775–805.
[60] L. Giraldo, A. Erto, J. Moreno-Piraján, Magnetite nanoparticles for removal of heavy metals from aqueous solutions: synthesis and characterization, Adsorption 19 (2013).
[61] M.P. Watts, V.S. Coker, S.A. Parry, R.A. Pattrick, R.A. Thomas, R. Kalin, J.R. Lloyd, Biogenic nano-magnetite and nano-zero valent iron treatment of alkaline Cr(vi) leachate and chromite ore processing residue, Appl. Geochem. 54 (2015) 27–42.
[62] C. Shan, Z. Ma, M. Tong, J. Ni, Removal of Hg(II) by poly(1-vinylimidazole)-grafted Fe_3O_4 @SiO_2 magnetic nanoparticles, Water Res. 69 (2015) 252–260.
[63] M.S.A. Mohamed, E. Mahmoud, A.E.H. Abdou, Enhanced removal of lead and cadmium from water by Fe_3O_4-cross linked-o-phenylenediamine nano-composite, Sep. Sci. Technol. 51 (2016) 237–247.
[64] H. Borji, G. Ayoub, R. Bilbeisi, N. Nassar, L. Malaeb, How effective are nanomaterials for the removal of heavy metals from water and wastewater? Water Air Soil Pollut. 231 (2020).
[65] A. Ali, H. Zafar, M. Zia, I. Haq, A. Phull, J. Sarfraz Ali, A. Hussain, Synthesis, characterization, applications, and challenges of iron oxide nanoparticles, Nanotechnol. Sci. Appl. 9 (2016) 49–67.
[66] C. Wang, L. Qiao, Q. Zhang, H. Yan, K. Liu, Enhanced cell uptake of superparamagnetic iron oxide nanoparticles through direct chemisorption of FITC-Tat-PEG600-b-poly(glycerol monoacrylate), Int. J. Pharm. 430 (2012) 372–380.
[67] T. Yu, C. Jiang, W. Wei, Z. Wu, W.-S. Kim, Recent progress on magnetic iron oxide nanoparticles: synthesis, surface functional strategies and biomedical applications, Sci. Technol. Adv. Mater. 16 (2015) 023501 (PMID:27877761).